Elimination of peak-locking error in PIV analysis using the correlation mapping method

J Chen and J Katz

Department of Mechanical Engineering, Johns Hopkins University, Baltimore,
MD 21218, USA

E-mail: katz@jhu.edu

Abstract

The peak-locking effect causes mean bias in most of the existing
cross-correlation based algorithms for PIV data analysis. This phenomenon
is inherent to the smooth curve-fitting through discrete correlation values,
which is used to obtain the sub-pixel part of the displacement. Almost all of
the existing effective methods to solve this problem require iterations. In this
paper we introduce a new technique for obtaining sub-pixel accuracy, which
bypasses the sub-pixel curve fitting, and eliminates the peak-locking effect,
but does not require iterations. The principles of the 'correlation mapping
method' (CMM) are based on the following logic: if one uses a bi-cubic
interpolation to express the second image based on the first one and the
unknown displacement, the correlation between them becomes a third-order
polynomial of the displacement, whose coefficients depend on the first
image. Matching this polynomial with the measured correlation provides an
equation for the displacement for each point of the correlation map. A
least-squares fit to the correlation values in the vicinity of the correlation
peak (e.g. 5×5 points) provides an estimate for the particle displacement,
including its sub-pixel part. We combine the new correlation mapping
method with corrections for particle image distortion (PID) to further reduce
the uncertainty in the velocity measurements. Three iterations typically
achieve converged results. The CMM-PID method is tested using synthetic
and experimental data. The peak-locking bias disappears in all cases. Even
the 'random' error is substantially smaller than that obtained using a
conventional sub-pixel curve fit. Issues related to streamline curvature and
uncertainty in estimates of velocity gradients are also discussed.

Keywords: particle image velocimetry, peak-locking error, image
interpolation, particle image distortion, correlation mapping

(Some figures in this article are in colour only in the electronic version)

1. Introduction

Particle image velocimetry (PIV) has become increasingly
popular over the past 15 years, and the principles of this
technique are already well documented, e.g. by Adrian (1991),
Westerweel (1997) and Raffel *et al* (1998). The accuracy of
PIV measurement depends on several factors, including the
properties of target flow fields, the properties and concentration
of seed particles, the optical setup, the data acquisition
system, the image interrogation technique, post-processing,
etc. Substantial efforts have already been invested in studying
the influence of these factors on the results and on the
improvements achieved by optimizing them. The error
introduced during image interrogation has received the most

attention since it provides the widest latitude for development of optimization tools (Keane and Adrian 1990, Westerweel 1997, Huang *et al* 1997, Lecordier *et al* 2001). International collaboration has also been organized to explore the benefit and deficiency of different processing techniques by analysing the same set of images (Stanislas *et al* 2003).

The uncertainties associated with PIV measurements can be classified into two categories: random error and bias error. The influence of random error can be reduced by statistical analysis using a sufficiently large ensemble set. The bias error, on the other hand, may still contaminate the results even after averaging (Huang *et al* 1997, Westerweel 1997, Christensen 2004), and typically generates a semi-regular, deterministic pattern in averaged results (Fincham and Spedding 1997). In the present study, we introduce an improved interrogation algorithm to eliminate the most significant bias error, the so-called 'peak-locking error'.

In a typical PIV measurement, we record two images, G_1 and G_2, with a time delay of Δt between them. To determine the displacement in a certain sub-section of the sample area, we select corresponding interrogation windows, g_1 and g_2, and calculate the cross-correlation function, $\varphi(m, n)$, defined as:

$$\varphi(m, n) = \sum_{i=1}^{M} \sum_{j=1}^{N} g_1(i, j) g_2(i + m, j + n) \qquad (1)$$

where M and N are the sizes of the interrogation window in pixels. The location of the peak in the distribution of $\varphi(m, n)$ gives the mean particle displacement within g_1. To achieve sub-pixel accuracy, a smooth curve is typically fitted through 3–4 points in the vicinity of the discrete correlation peak. We will refer to this procedure as sub-pixel curve fitting (SPCF). The commonly used methods include parabolic or Gaussian curve fits (e.g. Willert and Gharib (1991), Raffel *et al* (1998)). If the discrete peak is located at (m_p, n_p), a parabolic SPCF gives displacement, (U, V), of

$$\begin{cases} U = m_p + \dfrac{\varphi(m_p - 1, n_p) - \varphi(m_p + 1, n_p)}{2\varphi(m_p - 1, n_p) - 4\varphi(m_p, n_p) + 2\varphi(m_p + 1, n_p)} \\ V = n_p + \dfrac{\varphi(m_p, n_p - 1) - \varphi(m_p, n_p + 1)}{2\varphi(m_p, n_p - 1) - 4\varphi(m_p, n_p) + 2\varphi(m_p, n_p + 1)} \end{cases}$$
$$(2)$$

while a Gaussian SPCF gives

$$\begin{cases} U = m_p + \dfrac{\ln\varphi(m_p - 1, n_p) - \ln\varphi(m_p + 1, n_p)}{2\ln\varphi(m_p - 1, n_p) - 4\ln\varphi(m_p, n_p) + 2\ln\varphi(m_p + 1, n_p)} \\ V = n_p + \dfrac{\ln\varphi(m_p, n_p - 1) - \ln\varphi(m_p, n_p + 1)}{2\ln\varphi(m_p, n_p - 1) - 4\ln\varphi(m_p, n_p) + 2\ln\varphi(m_p, n_p + 1)} . \end{cases}$$
$$(3)$$

As has already been pointed out in several papers, such a curve fit causes a bias towards discrete values of displacement (Raffel *et al* 1998, Fincham and Spedding 1997, Christensen 2004), which is referred to as 'peak-locking error'. The displacement calculated using SPCF shows a strong preference towards integer values, and the error has a periodic pattern with a typical amplitude of 0.15 pixels that peaks at ± 0.25 pixels, as shown in figure 1. The peak-locking error increases when the diameter of the particle image is less than two pixels (Westerweel 1997). Such a bias causes substantial errors
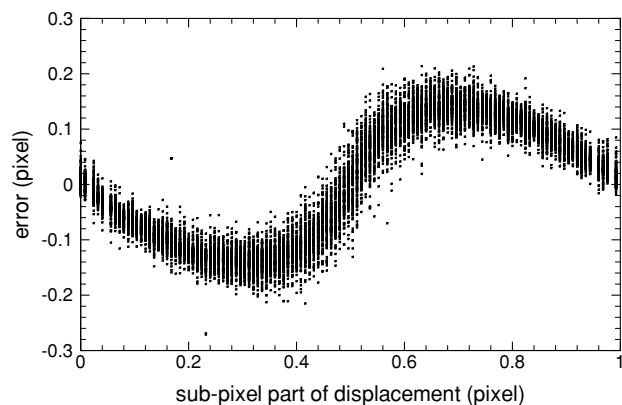
Figure 1. The distribution of the sub-pixel part of the error caused by using parabolic sub-pixel fitting while analysing a synthetically generated image of a stagnation point flow.

in mean derivatives, and as shown recently by Christensen (2004), significantly affects both the single and multi-point turbulence statistics.

Several methods have been proposed to remedy the peak-locking effect. For example, Roesgen (2003) explored the optimal sub-pixel interpolation scheme and recommended using a *Sinc* function. Several papers have introduced methods, which are based on increasing the image size artificially by interpolation of pixel values, and by applying the sub-pixel peak fitting to the refined correlation maps instead of the original coarse grids. Lecordier *et al* (1999) proposed an iterative grid refinement method; Gui and Wereley (2002) applied continuous window shifting; Wereley and Gui (2003) and Gui and Seiner (2004) proposed a central difference image correction method. Fincham and Delerce (2000) introduced a peak anti-aliasing, spline transformed interrogation scheme, which also involves interpolation, but does not involve sub-pixel fitting to the correlations. These methods seem to be effective to varying degrees, but cause substantial increase in data processing time. Roth and Katz (2001) attempted to utilize sub-pixel histogram equalization as a post-processing step. This method artificially removes the periodic pattern of the bias but lacks any physical support.

In this paper, we introduce a new approach to eliminate the peak-locking error that bypasses the sub-pixel curve fitting operation, and does not require artificial window enlargement and/or iterations, at least as long as we do not correct for window deformation. The principles of this method are presented in detail in section 2. Treatment of distorted interrogation windows is discussed in section 3. In section 4, we report an implementation of the new method on different synthetic and experimental images. The results are compared with those of parabolic and Gaussian SPCF methods.

2. The correlation mapping method

2.1. Principles of the technique

The local displacement (U, V) can be decomposed into an integer part, $(u_{\text{int}}, v_{\text{int}})$, and a sub-pixel part, (u, v), i.e. $0 \leqslant u, v < 1$ (pixels). For simplicity, in the following analysis we focus on the sub-pixel part. During analysis, the

integer part of the displacement can be easily determined by finding the location of the peak in the discrete correlation map. Under ideal conditions, i.e. no particle pattern distortion, no out-of-plane motion and no noise, the intensity distribution in the second interrogation window, g_2, is uniquely determined by the first window, g_1, and the local displacement. Thus, $\varphi(m, n)$ is uniquely determined by g_1 and (U, V). During a virtual displacement of (u', v'), the virtual second exposure, $g_{2'}$, is:

$$g_{2'}(i, j) = g_1(i - u', j - v') \qquad (4)$$

and, the virtual correlation between g_1 and $g_{2'}$, $\varphi'(m, n)$, is

$$\varphi'(m, n, u', v') = \sum_{i=1}^{M} \sum_{j=1}^{N} g_1(i, j) g_1(i - u' + m, j - v' + n). \qquad (5)$$

As the virtual displacement approaches the real one, $\varphi'(m, n, u, v)$ approaches $\varphi(m, n)$. Thus, the real displacement can be found by minimizing the difference between $\varphi(m, n)$ and $\varphi'(m, n, u, v)$. Since the equality between φ and φ' applies to every point on the correlation map, one obtains a series of equations with u and v as unknowns. We obtain an 'optimal' value for u and v by using a least-squares fit to minimize the difference between φ and φ' in the vicinity of the correlation peak. To successfully implement this approach, the following questions need to be answered: (i) How to construct the virtual second exposure, $g_{2'}$, and from it, the value of φ'; (ii) How to minimize the difference between φ and φ', which provides the optimal value of the displacement.

2.2. Construction of $g_{2'}$ by sub-pixel image interpolation

Equation (4) is a sub-pixel image interpolation problem. This topic has been addressed in many digital image processing books, e.g. Bracewell (1995) and Teuber (1993), and has been applied extensively in iterative image deformation methods for PIV analysis, e.g. Scarano (2002) and Stanislas *et al* (2003). The popular interpolation schemes range from first- to fourth-order two-dimensional polynomials, to a Cardinal Sinc function, to a cubic-spline interpolation, etc. As addressed in many studies, a good sub-pixel interpolation scheme should avoid loss, addition and biasing of image information (e.g. Scarano 2002). For the specific application in PIV, the centre location of the interpolated particle must be accurately reproduced without bias. In this paper, we examine the effectiveness of first- to third-order polynomials, i.e. bi-linear, bi-parabolic and bi-cubic interpolations. Figure 2 shows the pixels involved in these interpolation methods to obtain the greyscale value at $(p + u', q + v')$ from neighbouring values at integer locations. Since the discussion of the inherent inaccuracies associated with each method is not the main issue of this paper, we provide the details on the process of evaluating them in appendix A.

Of the three above-mentioned methods, the bi-cubic interpolation has the least bias when the sub-pixel displacement is less or more than 0.5. Thus, we opt to proceed
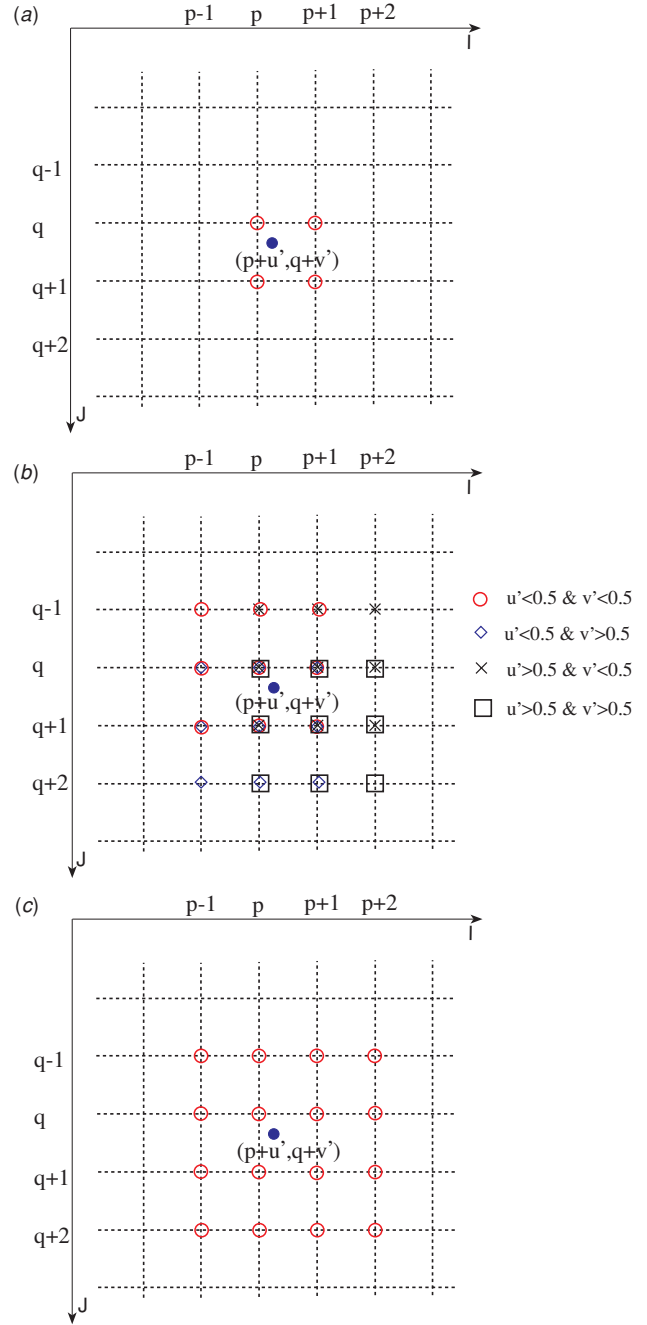

Figure 2. Pixels involved in different image interpolation schemes. (*a*) Bi-linear, (*b*) bi-parabolic and (*c*) bi-cubic.

using bi-cubic image interpolation, i.e.

$$\begin{aligned} g(p + u', q + v') &= C_1^{(p,q)} \cdot u'^3 \cdot v'^3 + C_2^{(p,q)} \cdot u'^3 \cdot v'^2 \\ &+ C_3^{(p,q)} \cdot u'^2 \cdot v'^3 + C_4^{(p,q)} \cdot u'^2 \cdot v'^2 + C_5^{(p,q)} \cdot u'^3 \cdot v' \\ &+ C_6^{(p,q)} \cdot u' \cdot v'^3 + C_7^{(p,q)} \cdot u'^3 + C_8^{(p,q)} \cdot v'^3 \\ &+ C_9^{(p,q)} \cdot u'^2 \cdot v' + C_{10}^{(p,q)} \cdot u' \cdot v'^2 + C_{11}^{(p,q)} \cdot u'^2 \\ &+ C_{12}^{(p,q)} \cdot v'^2 + C_{13}^{(p,q)} \cdot u' \cdot v' + C_{14}^{(p,q)} \cdot u' \\ &+ C_{15}^{(p,q)} \cdot v' + C_{16}^{(p,q)}. \end{aligned} \qquad (6)$$

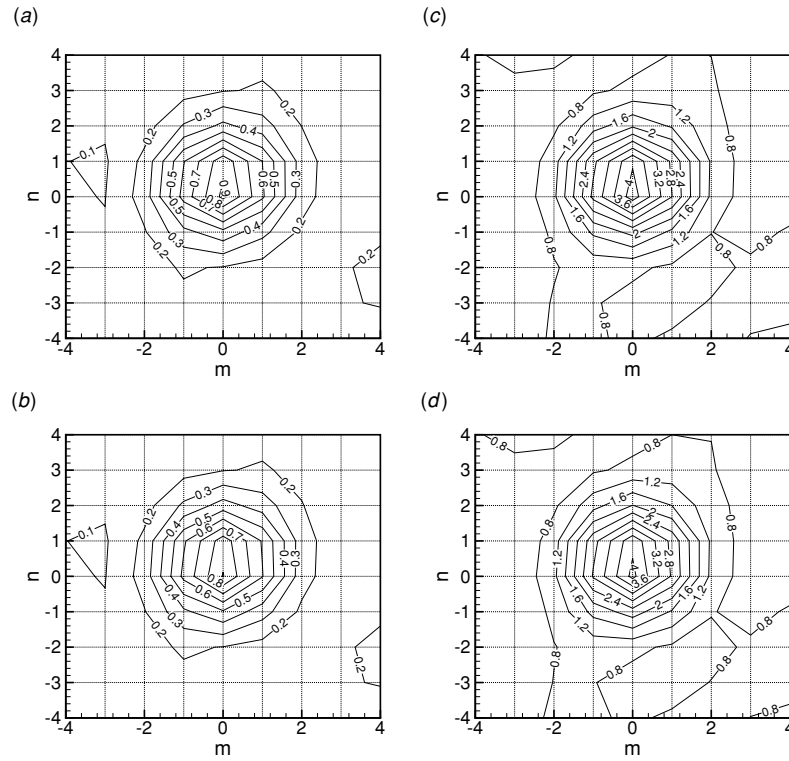Specific values for the coefficients, C_k, are provided in appendix B.

Figure 3. (*a*) Exact correlation map $\varphi(m, n)$ for a displacement of (0.0, 0.4), (*b*) bi-cubically interpolated virtual correlation map $\varphi'(m, n)$ with the same displacement, (*c*) $\varphi(m, n)/\overline{\varphi}$ and (*d*) $\varphi'(m, n)/\overline{\varphi'}$.

2.3. Matching of correlation map

This section examines the relationship between $\varphi(m, n)$ and $\varphi'(m, n)$, while focusing only on the sub-pixel part of the displacement. Figure 3 compares $\varphi(m, n)$ to $\varphi'(m, n)$ in the vicinity of the correlation peak of a 32×32 pixel window using synthetic image pairs with uniform particle displacement of (0.0, 0.4), and bi-cubic interpolation (equation (6)) to calculate $\varphi'(m, n)$. The first window, g_1, contains randomly distributed Gaussian particles, with mean diameter, d_p, of 2.4 pixels, at a concentration of 0.03 particles per pixel. Clearly $\varphi'(m, n)$ captures almost all the features of $\varphi(m, n)$ when the estimated displacement (u', v') approaches the exact one (u, v). However, the virtual correlation peak is slightly lower than the exact value due to the interpolation error discussed in appendix A. To correct this problem, we normalize both correlation maps with their mean values, and then match the values of $\varphi(m, n)/\overline{\varphi}$ with those of $\varphi'(m, n)/\overline{\varphi'}$ at every (m, n), where the overbar denotes averaging over all (m, n). The effect of normalization is illustrated in figures 3(*c*) and (*d*). Normalizing the peaks reduces the difference between the original and interpolated peaks. However, subsequent tests have indicated that the normalization has minimal impact on the velocity measurements, and the method works equally well without it.

For a bi-cubic interpolation, substituting equation (6) into equation (5), one obtains

$$\varphi'_C(m, n, u', v') = \Phi_{C_1}^{(m,n)} \cdot u'^3 \cdot v'^3 + \Phi_{C_2}^{(m,n)} \cdot u'^3 \cdot v'^2$$
$$+ \cdots + \Phi_{C_{16}}^{(m,n)} \tag{7}$$

where the 16 coefficients are

$$\begin{cases} \Phi_{C_k}^{(m,n)} = \sum_{i=1}^{M} \sum_{j=1}^{N} g_1(i, j) \cdot C_k^{(i+m, j+n)} \\ k = 1, 2, \ldots, 16. \end{cases} \tag{8}$$

One should attempt to minimize the difference between $\varphi(m, n)$ and $\varphi'(m, n)$ around the correlation peak. In the present paper, we focus on a 5×5 pixel area, where the most useful information exists. The choice of 5×5 pixels is somewhat arbitrary, and larger areas can also be used. To find the 'optimal' values of u and v, we use a least-squares fit that minimizes the difference between the virtual and exact correlation values. The procedure consists in finding (u', v') that minimizes the squared residue, $\varepsilon(u', v')$, defined as:

$$\varepsilon(u', v') = \sum_{m=-2}^{2} \sum_{n=-2}^{2} \left(\frac{\varphi(m, n)}{\overline{\varphi}} \right.$$

$$\left. - \frac{\Phi_{C_1}^{(m,n)} \cdot u'^3 \cdot v'^3 + \Phi_{C_2}^{(m,n)} \cdot u'^3 \cdot v'^2 + \cdots + \Phi_{C_{16}}^{(m,n)}}{\overline{\Phi_{C_1}^{(m,n)} \cdot u'^3 \cdot v'^3} + \overline{\Phi_{C_2}^{(m,n)} \cdot u'^3 \cdot v'^2} + \cdots + \overline{\Phi_{C_{16}}^{(m,n)}}} \right)^2 . \tag{9}$$

Other approaches are also possible, e.g. by creating some bias favouring high correlation values. In the present study, we use an increment of 0.01 pixel in u' and v' to find the minimal residue. For the purpose of comparison, the same procedure is also used with the bi-parabolic and bi-linear interpolations. Since the procedure introduced here attempts to minimize the combined errors of all the correlation values around the peak, we refer to it as the correlation mapping method (CMM).

In summary, application of CMM, using bi-cubic interpolation, consists of the following steps:

(1) Calculating $\varphi(m, n)$ for a given interrogation window.
(2) Determining the integer part of the measured displacement, (u_{int}, v_{int}), based on the location of the discrete peak of $\varphi(m, n)$.
(3) Calculating the coefficients of φ', $\Phi_{C_k}^{(m,n)}$ using equation (8) and appendix B, based on the values of g_1 around (u_{int}, v_{int}).
(4) Finding the optimal values of u' and v', u_{opt} and v_{opt}, that minimize the squared residue defined in equation (9).
(5) The total displacement is $(u_{int} + u_{opt}, v_{int} + v_{opt})$.

Compared with the other remedies to peak-locking, which are discussed briefly in the introduction, the correlation mapping method does not involve sub-pixel curve fitting, and does not require a refined grid. Furthermore, depending on the selected area, it can match the entire vicinity of the correlation peak. Before proceeding with examples of implementation, the next section combines CMM with methods that correct for particle image deformation.

3. Particle image distortion

In a flow field with high velocity gradients, the relative position of particle patterns contained in the interrogation window changes between exposures. As a result, the correlation peak broadens, deforms or becomes fragmented, degrading the measurement accuracy. To solve this problem, Huang *et al* (1993) introduced the particle image distortion (PID) technique. Similar methods have been discussed since then in many papers, e.g. Lin and Perlin (1998), Hart (2000), Scarano and Riethmuller (2000), Nogueira *et al* (2001), Wereley and Meinhart (2001), Florio *et al* (2002), Stanislas *et al* (2003), Scarano (2002), Wereley and Gui (2003), and Gui and Seiner (2004). In the present study, we combine the correlation mapping method with PID, abbreviated here as CMM-PID.

The application of CMM-PID can be summarized as:

(1) CMM is first applied without distortion correction to obtain the first iteration of the displacement $(U, V)_1$.
(2) The local displacement gradients, $\partial U/\partial x$, $\partial U/\partial y$, $\partial V/\partial x$ and $\partial V/\partial y$, are determined using a 5-point least-squares finite-difference scheme (Raffel *et al* 1998, Foucaut and Stanislas 2002).
(3) Every pixel within the interrogation window is shifted with respect to the window centre (x_c, y_c), creating another image, g_1', whose greyscale distribution is

$$g_{1'}(x, y) = g_1(x - \delta U(x, y), y - \delta V(x, y)) \quad (10)$$

where, using a first-order approximation,

$$\begin{cases} \delta U(x, y) \simeq \left.\dfrac{\partial U}{\partial x}\right|_{(x_c, y_c)} (x - x_c) + \left.\dfrac{\partial U}{\partial y}\right|_{(x_c, y_c)} (y - y_c) \\[2ex] \delta V(x, y) \simeq \left.\dfrac{\partial V}{\partial x}\right|_{(x_c, y_c)} (x - x_c) + \left.\dfrac{\partial V}{\partial y}\right|_{(x_c, y_c)} (y - y_c). \end{cases} \quad (11)$$

Bi-cubic interpolation is used to determine the values of g_1 between discrete pixels.

(4) Step 1 is repeated, using images g_1' and g_2 to obtain the result of the next iteration $(U, V)_2$. This process is repeated until the results converge.
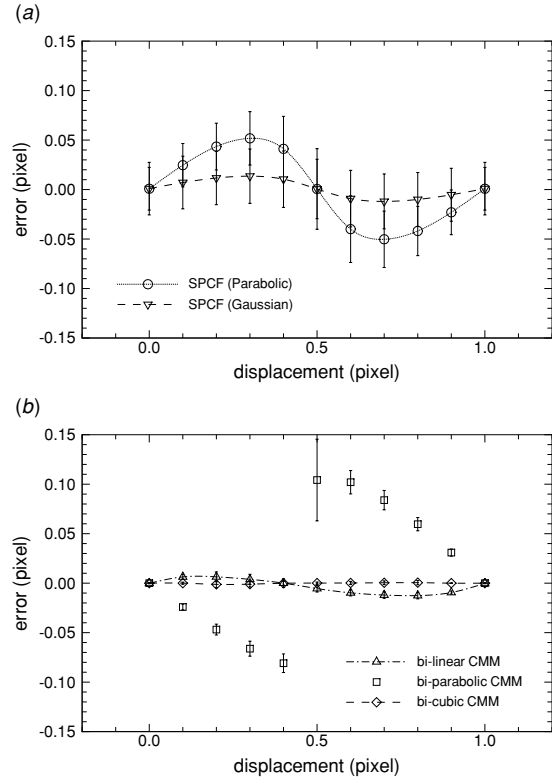

Figure 4. Error of uniformly translated image pairs: (*a*) 3-point parabolic and Gaussian SPCF; and (*b*) CMM with different interpolation methods. Symbol: mean error. Error bar: rms error.

4. Applications and uncertainty analysis

4.1. Analysis of synthetic images

The correlation mapping method is applied to several PIV images, both synthetic and experimental. The results are compared with the exact values as well as with the output of sub-pixel curve fitting methods (equations (2) and (3)). The synthetic image pairs are generated by randomly distributing Gaussian particles in the first image at a mean number density of 0.03 particles per pixel. The particle diameters and peak intensities have random Gaussian distributions with a mean diameter of 2.4 pixels and mean greyscale of 190. The second exposure is obtained by shifting the particles according to the simulated displacement pattern. The greyscales in the particles of the second exposure also have Gaussian distributions, i.e. we do not interpolate the first image to generate the second image.

To expedite the processing, we first determine the location of the discrete correlation peak using a typical correlation software discussed in Roth *et al* (1999) and Roth and Katz (2001), and then use CMM to determine the sub-pixel value. For all the results presented in this section, the interrogation window size is 32×32 pixels, and the vector spacing is 16 pixels (50% overlap).

Starting with 256×256 pixel synthetic images simulating a uniform translation of 0.0 to 1.0 pixels, CMM with bi-linear, bi-parabolic and bi-cubic interpolations is compared to SPCF. The errors are summarized in figure 4. It is evident that both SPCF methods give a biased result, with the amplitude of the
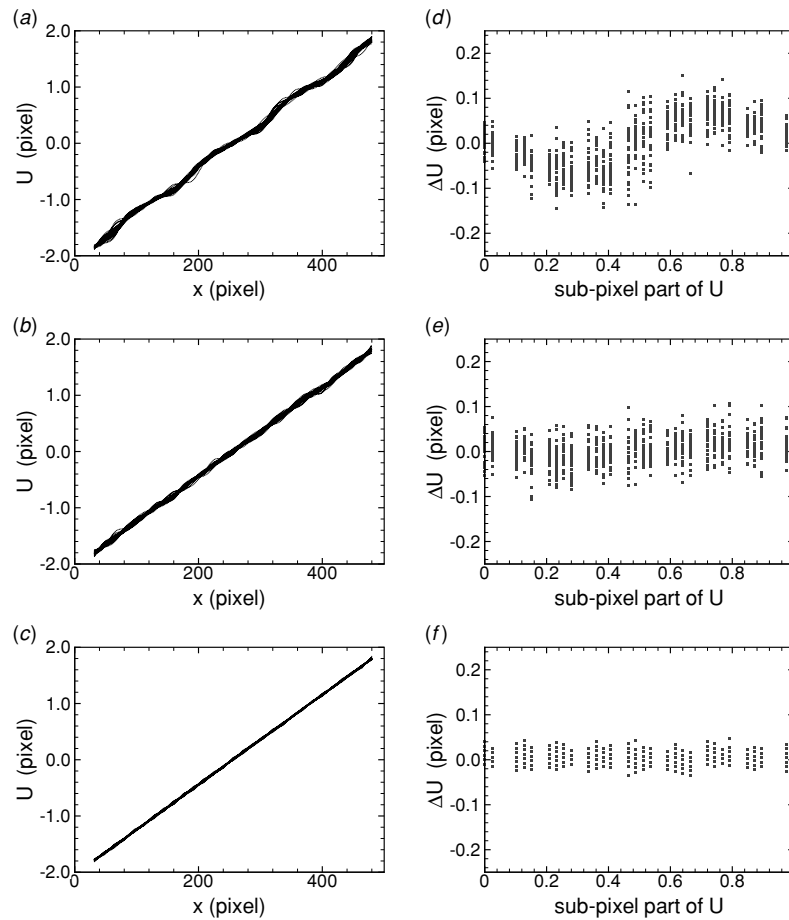
Figure 5. (*a*)–(*c*) Horizontal displacement along the *x*-direction, and (*d*)–(*f*) the corresponding error (ΔU) versus the sub-pixel part of *U*, obtained from analysis of synthetic images simulating a stagnation point flow. (*a*) and (*d*) Parabolic SPCF, (*b*) and (*e*) Gaussian SPCF, and (*c*) and (*f*) bi-cubic CMM.

mean error associated with the Gaussian fit being lower than that of the parabolic fit. The same trend is also reported in Scarano and Riethmuller (2000) and Roesgen (2003). The bi-parabolic CMM gives the worst mean bias, even compared to the SPCF results. This error is caused by an inherent bias in the interpolation of images, as described in appendix A. The abrupt change in magnitude and sign of the error is caused by a change in the pixels used in the bi-parabolic interpolation when the sub-pixel displacement crosses 0.5 (figure 2(*b*)). Conversely, the bi-linear CMM shows a significant improvement with only a slight bias with a magnitude of about 0.01 pixel. This very small error is also caused by an interpolation error. The bi-cubic CMM seems to eliminate the mean peak-locking bias completely. Both the bi-linear CMM and bi-cubic CMM reduce the rms values of the error significantly from 0.02–0.04 pixels in the SPCF data to 0.000–0.003 pixels. Based on this trend, the bi-cubic scheme is chosen as the only interpolation method in the following applications of CMM.

Synthetic stagnation point flow is another ideal case to validate PIV analysis algorithms, due to the linearity of the velocity profile. Figure 5 compares the results of SPCF and bi-cubic CMM using 1024×1024 pixel synthetic image pairs simulating a stagnation point flow with $\partial U / \partial x = 0.008$. In this case, we do not use PID corrections. Clearly, the bi-cubic CMM gives a smoother velocity profile, without

the semi-regular deterministic error pattern that characterizes both SPCF methods, i.e. it successfully eliminates the peak-locking effect. The rms value of the CMM error, $\sigma_{\Delta u}$, is $\sim$ 0.01 pixels, while the values of both SPCF methods are about 0.04 pixels.

4.2. Analysis of Oseen vortex images

Huang *et al* (1993) applied the PID technique on synthetic Oseen vortex images, with the following tangential and radial displacements:

$$
\begin{cases}
u_\theta(r, \theta) = \dfrac{\Gamma}{2\pi r} \left[1 - \exp\left(-\dfrac{r^2}{4\nu t} \right) \right] \cdot \Delta t \\
u_r(r, \theta) = 0.
\end{cases}
\tag{12}
$$

Thus, we also apply the bi-cubic CMM-PID on Oseen vortex images with $\Gamma = 750\,000$ (pixel)^2/s, $\Delta t = 0.02$ s and $\nu t = 7500$ (pixel)^2. Again, the image size is 1024×1024 pixels. Figures 6 and 7 compare the exact values of u_θ and u_r with the ones calculated using SPCF (Gaussian) without PID and using CMM-PID, respectively. The improvements with PID iterations are also presented. It is evident that CMM-PID is much more accurate than SPCF, and that the uncertainty decreases with PID iterations. Figure 8 compares the pdfs of errors in horizontal displacement over the entire image. The
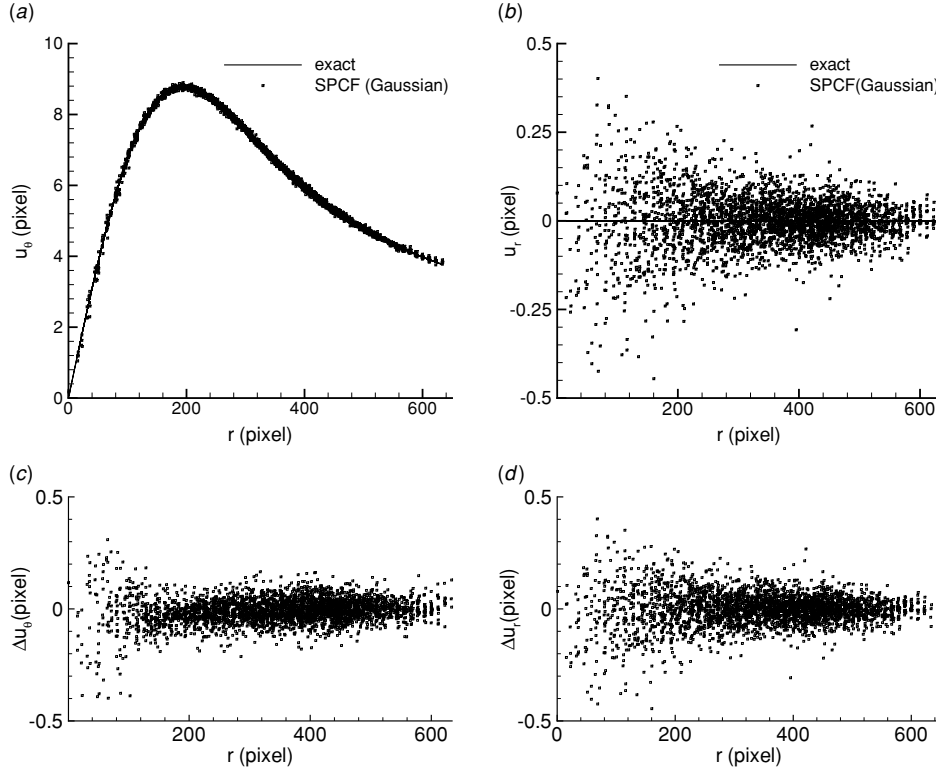
Figure 6. Results of analysing an Oseen vortex using Gaussian sub-pixel curve fitting: (*a*) u_θ, (*b*) u_r, (*c*) error in u_θ, Δu_θ and (*d*) error in u_r, Δu_r.

CMM-PID results seem to converge quickly, as determined by the very little difference between the second and third iterations. The rms values of the error for the different methods are: 0.08 pixels for parabolic SPCF, 0.07 pixels for Gaussian SPCF, 0.06 pixels for CMM-PID iteration 1, 0.01 pixels for CMM-PID iteration 2 and 0.01 pixels for CMM-PID iteration 3. The removal of peak-locking bias in the CMM-PID results is demonstrated in figure 9.

Examination of the error in figures 7(*e*) and (*g*) reveals a small negative bias of u_θ that peaks around $r = 150$, with a maximum magnitude of 0.04 pixels. To identify the source of this bias error, the flow simulated by the Oseen vortex images is decomposed into two elements: one simulating a pure solid body rotation, and the other simulating a 1D planar flow, which has a displacement profile similar to that in equation (12), i.e.

$$
\begin{cases}
U(x, y) = \dfrac{\Gamma}{2\pi(y + 0.5)} \left[1 - \exp\left(-\dfrac{(y + 0.5)^2}{4\nu t} \right) \right] \cdot \Delta t \\
V(x, y) = 0.
\end{cases}
\tag{13}
$$

We refer to the latter as a 'planar Oseen flow'. This procedure separates the effects of streamline curvature from the curvature of the displacement distribution.

The CMM-PID results of the solid body rotation images do not reveal any bias, and the uncertainty of the third iteration is about 0.01 pixels (not shown). The results for the planar Oseen images are shown in figure 10. When the PID is applied using a first-order approximation for the deformation (equation (11)), the bias occurs in the region with significant curvature (figure 10(*b*)), as one may note by comparing it

with the distribution of dU/dy. If one adopts a second-order distortion correction in PID, i.e. replaces equation (11) with:

$$
\begin{cases}
\delta U(x, y) \simeq \left.\dfrac{\partial U}{\partial x}\right|_{(x_c, y_c)} (x - x_c) + \left.\dfrac{\partial U}{\partial y}\right|_{(x_c, y_c)} (y - y_c) \\
\quad + \dfrac{1}{2} \left.\dfrac{\partial^2 U}{\partial x^2}\right|_{(x_c, y_c)} (x - x_c)^2 + \left.\dfrac{\partial^2 U}{\partial x \partial y}\right|_{(x_c, y_c)} (x - x_c)(y - y_c) \\
\quad + \dfrac{1}{2} \left.\dfrac{\partial^2 U}{\partial y^2}\right|_{(x_c, y_c)} (y - y_c)^2 \\[2ex]
\delta V(x, y) \simeq \left.\dfrac{\partial V}{\partial x}\right|_{(x_c, y_c)} (x - x_c) + \left.\dfrac{\partial V}{\partial y}\right|_{(x_c, y_c)} (y - y_c) \\
\quad + \dfrac{1}{2} \left.\dfrac{\partial^2 V}{\partial x^2}\right|_{(x_c, y_c)} (x - x_c)^2 + \left.\dfrac{\partial^2 V}{\partial x \partial y}\right|_{(x_c, y_c)} (x - x_c)(y - y_c) \\
\quad + \dfrac{1}{2} \left.\dfrac{\partial^2 V}{\partial y^2}\right|_{(x_c, y_c)} (y - y_c)^2
\end{cases}
\tag{14}
$$

the bias disappears, as demonstrated in figure 10(*c*). Thus, the aforementioned bias in Oseen vortex results occurs in the region where a first order approximation is insufficient to correct for window deformation. This conclusion has also been confirmed by varying the velocity gradient in the vortex core. As shown in figure 11, the bias with linear PID increases with second order derivative, i.e. deceasing radius of curvature, but it disappears if one utilizes a second order PID correction. At least for the profile in equation (13), the bias exceeds the
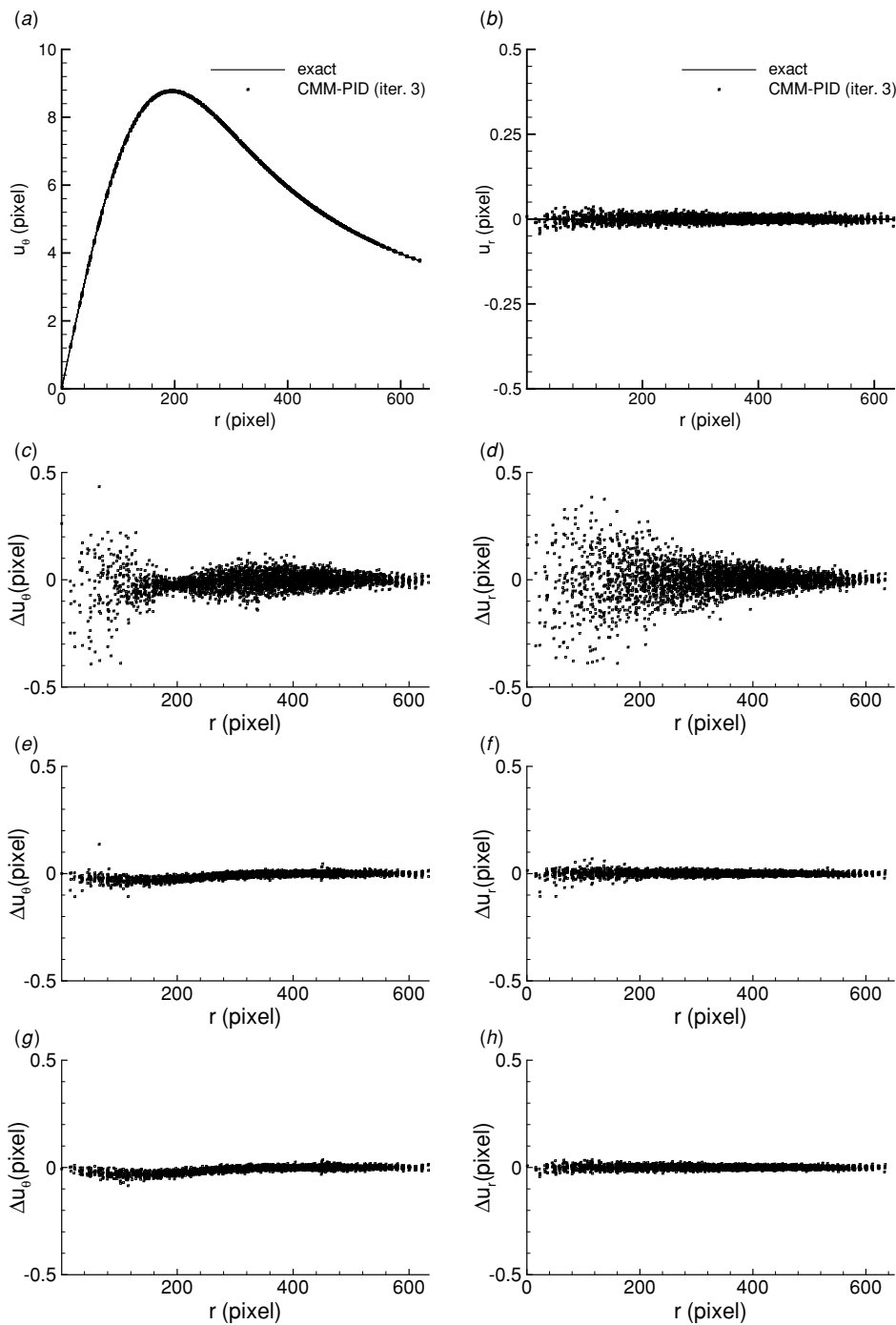
Figure 7. Results of CMM-PID analysis of Oseen vortex images: (*a*) and (*b*) u_θ and u_r for iteration 3, respectively; (*c*) and (*d*) Δu_θ and Δu_r of PID iteration 1; (*e*) and (*f*) Δu_θ and Δu_r of PID iteration 2; and (*g*) and (*h*) Δu_θ and Δu_r of PID iteration 3.

present ± 0.01 pixel scatter level when $\delta \cdot \mathrm{d}^2 U/\mathrm{d}y^2 > 0.01$, where δ is the size of the interrogation window.

The displacement errors in figure 10(*c*) range from -0.01 to $+0.01$ pixels. The limits of this scatter are equal to the presently selected resolution for the bi-cubic interpolation scheme and least-squares fit, both of which have resolutions of 0.01 pixels. This error range can be further reduced by using a higher resolution, of course at the cost of increasing processing time. Sample tests using a resolution of 0.002 pixels reduce the scatter range by five times (results not shown).

4.3. Application of CMM-PID to experimental flow images

Bi-cubic CMM is also implemented to analyse experimental data of a turbulent flow. The 2048 × 2048 pixels images of a nearly homogeneous isotropic turbulence flow field with weak mean velocity are recorded under the experimental conditions described in Chen *et al* (2005). Figure 12 presents the measured velocity field. It contains 121 × 121 velocity vectors calculated using 32 × 32 pixel interrogation windows. The mean diameter of particle images is about 3.0 pixels. Since we do not know the exact results, the data are evaluated using
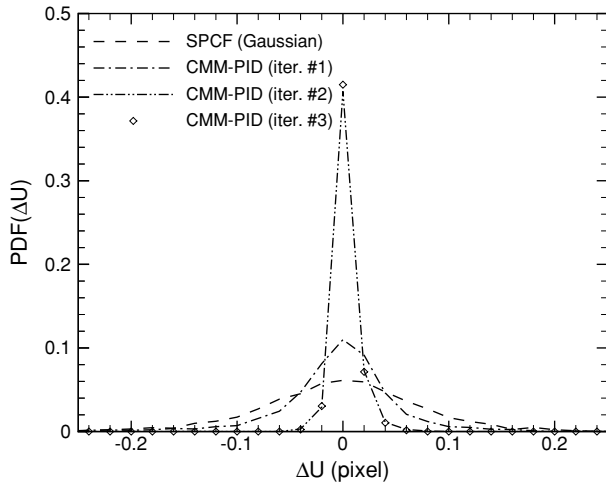
Figure 8. PDF of measurement error for a synthetic Oseen vortex. Note that the results for the second and third iterations overlap.
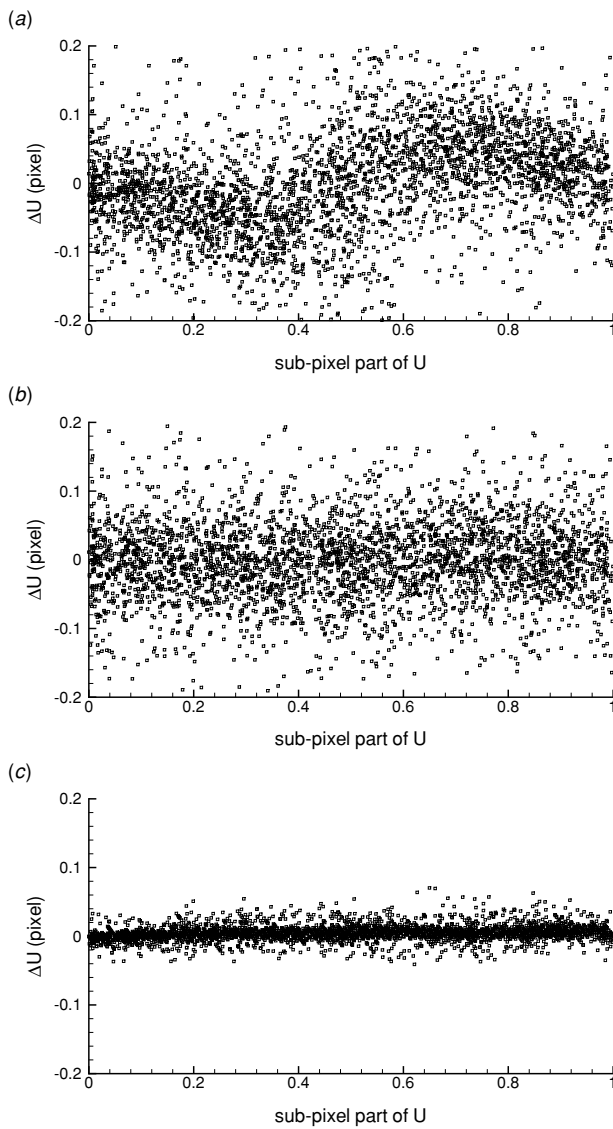

Figure 9. Error versus exact sub-pixel displacement for a synthetic Oseen vortex: (*a*) parabolic SPCF, (*b*) Gaussian SPCF and (*c*) CMM-PID (iteration 3).
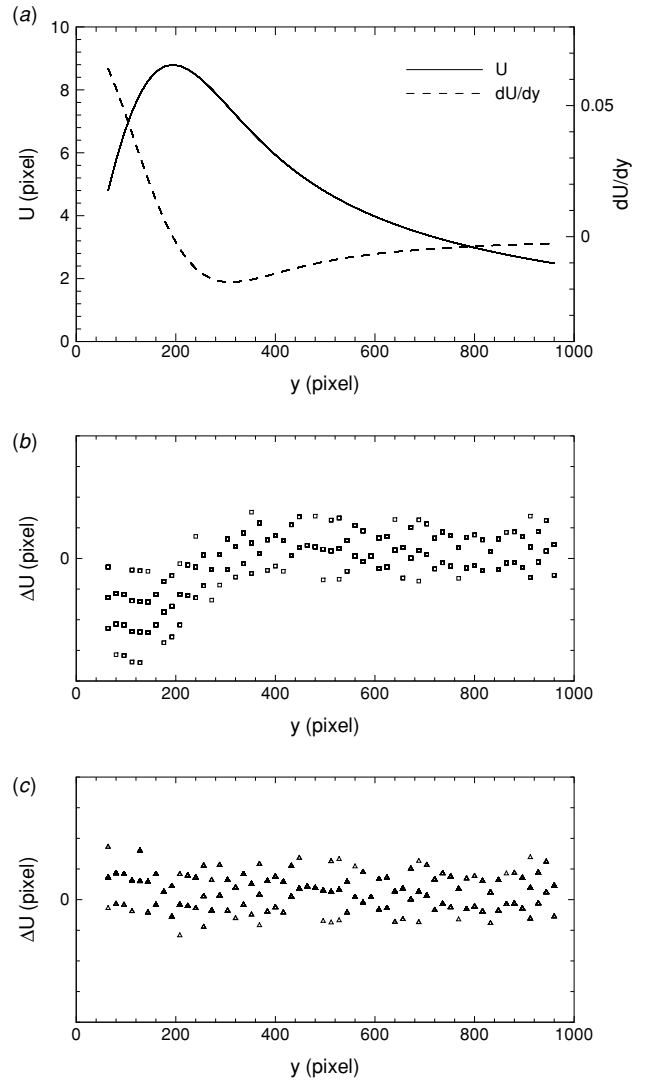

Figure 10. The synthetic planar Oseen (equation (13)) results: (*a*) U and dU/dy (exact values), (*b*) error of CMM+PID, with first-order correction for deformation, and (*c*) error of CMM+PID with second-order correction for deformation.
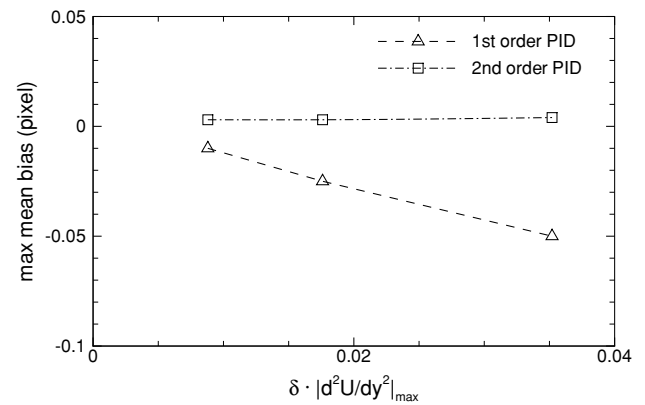

Figure 11. Mean bias versus radius of curvature of the simulated planar Oseen flow (equation (13)). δ is the interrogation window size.
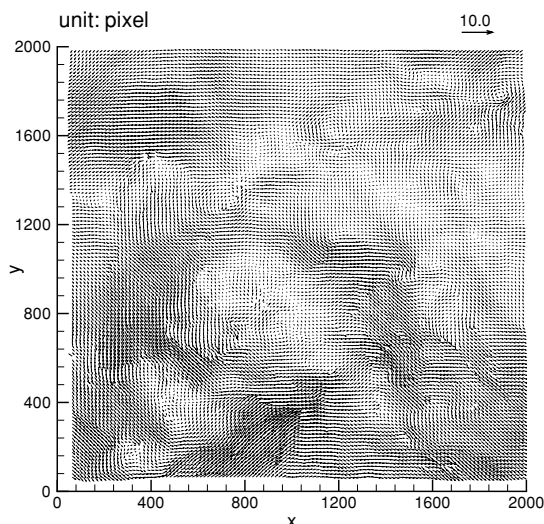
Figure 12. An experimental velocity field of turbulent flow analysed using CMM-PID, iteration 3.
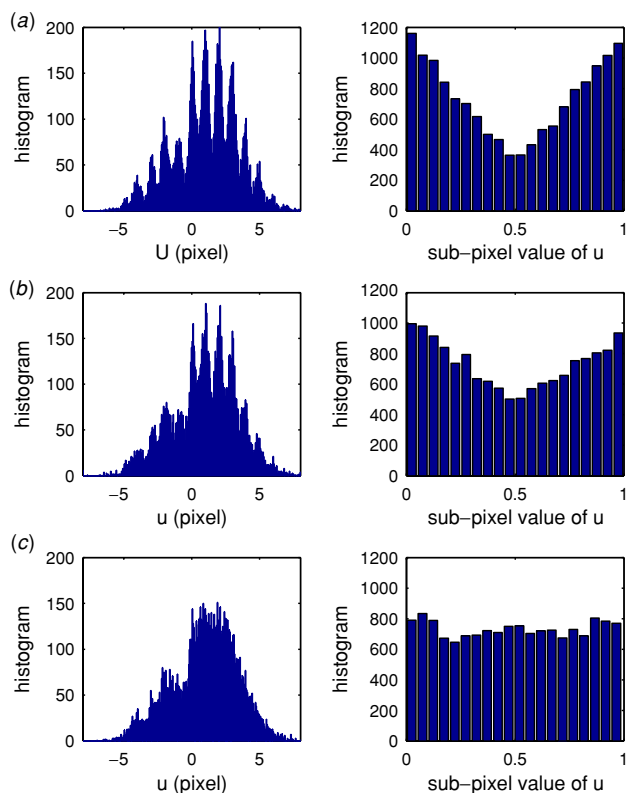

Figure 13. Histograms of the measured horizontal displacement component (left) and its sub-pixel part (right) of the experimental turbulent flow shown in figure 12. The bin size is 0.05 pixels. (*a*) Parabolic SPCF, (*b*) Gaussian SPCF and (*c*) CMM-PID (iteration 3) with first-order distortion correction.

histograms of measured displacement and its sub-pixel part, shown in figure 13. The bias towards integer values is evident in both SPCF histograms, but does not exist in the CMM-PID data.

Next, 2048 × 2048 pixel experimental PIV images obtained in a circular Couette flow facility (unpublished work by van Hout *et al*) are analysed using both SPCF and CMM-
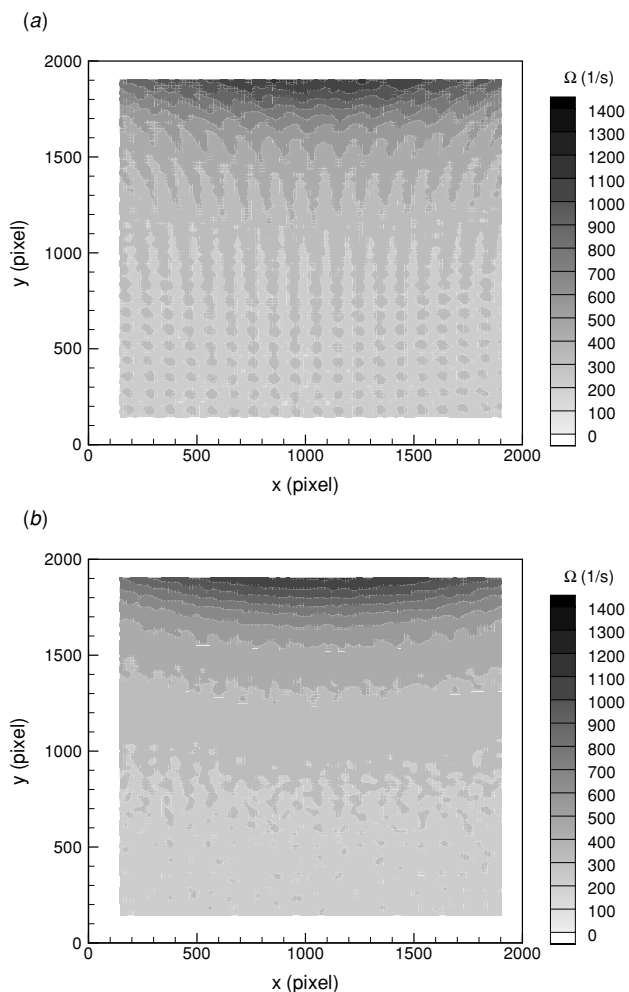
Figure 14. Average vorticity distribution of an experimental Couette flow obtained based on analysis of five image pairs using (*a*) parabolic SPCF and (*b*) CMM-PID (iteration 3) with first-order distortion correction.

PID. The window and particle size are the same as the first sample. In this set the tangential displacement varies from 0 to 50 pixels over the field of view, indicating the existence of strong velocity gradients. The typical distortion within a single interrogation window is about 1 pixel. The histograms of measured displacements are similar to those shown in figure 13 and thus not shown. The vorticity, $\Omega = \partial U/\partial y - \partial V/\partial x$, calculated using a second-order finite differencing, and averaged over five images, is shown in figure 14. The well-organized chequered pattern in the SPCF results, with amplitudes of oscillation reaching 35% of the local values, is caused by the peak-locking error. Conversely, one can detect only a very slight pattern in the CMM-PID data, with amplitude of about 5% of the local values. Clearly, use of CMM-PID causes a substantial improvement in the accuracy of the vorticity measurements.

In an attempt to identify the origin of the slight pattern in the CMM-PID data, we also calculate and examine vorticity distributions of the synthetic Oseen vortex (equation (12)). The distributions of error in vorticity along the centre line of the vortex, shown in figure 15, clearly indicate that the CMM-PID errors are caused by discretization, i.e. by using
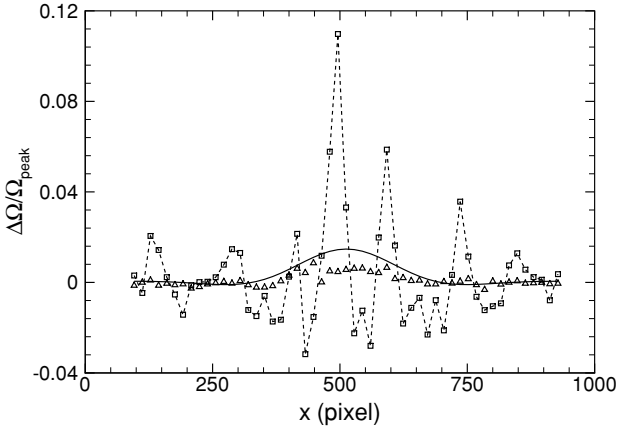
Figure 15. Error in calculating the vorticity distribution, $\Delta\Omega = \Omega - \Omega_{\text{exact}}$, in a synthetic Oseen vortex (equation (12)), along a line crossing the vortex core. Squares and dashed line: SPCF, triangles: CMM-PID 3, and solid line: second-order finite differencing of the exact velocity components.

second-order finite differencing to estimate the vorticity. In fact, the distribution of CMM-PID error is almost equal to that obtained from second-order finite differencing using the exact values of the velocity.

4.4. Effect of background noise

The experimental images are often contaminated by noise, introduced by different sources (e.g. Bracewell 1995). To test the application of the correlation mapping method in the presence of background noise, we added random Gaussian noise to the synthetic images simulating a high-shear planar Couette flow. For moderately contaminated synthetic images, i.e. with a noise variance of 0.001, the rms errors of SPCF and CMM-PID are 0.07 and 0.02 pixels, respectively. For heavily contaminated images, with a noise variance of 0.005, SPCF gives a rms error of 0.08 pixels, while the rms error of CMM-PID is 0.04 pixels. In both cases, the CMM-PID results are still better than those of SPCF. However, this analysis is preliminary. Examination of noisy images along with effects of out-of-plane motion will continue, and be addressed in further publications.

5. Summary and conclusions

A new approach, the correlation mapping method, is introduced in order to improve the sub-pixel accuracy, and eliminate (or at least greatly reduce) the peak-locking effect in PIV analysis. Using sub-pixel interpolation, this method expresses the second exposure of an interrogation window as a polynomial function with unknown displacement, whose coefficients are determined by the greyscale distribution of the first image. Thus, the correlation between this function and the first exposure is also a polynomial of the displacement. This virtual correlation function can be matched with the exact correlation value at every point in the correlation map. A least-squares method is used to find the optimal displacement components that minimize the difference between the real and virtual correlation values in a 5×5 pixel area surrounding the discrete correlation peak. This method bypasses the smooth

sub-pixel curve-fitting in finding the correlation peak. Of the three polynomial sub-pixel image interpolation methods examined in this paper, the bi-cubic method provides the best results. One may select other, more accurate, fitting methods, such as Gaussian fitting, but we examine the new procedure using the bi-cubic fit.

The CMM is also incorporated with the iterative PID method to account the local velocity gradient. The combined CMM-PID achieves further improvements in accuracy, along with fast convergence after two to three iterations. In regions with substantial curvature in displacement profile, a first-order approximation for the image deformation becomes insufficient, and it is necessary to apply PID using a second-order correction. The bias using a first-order PID diminishes with increasing radius of curvature of the displacement profile. However, a radius of curvature smaller than 100 times the interrogation window size creates a bias that exceeds the interpolation scatter of 0.01 pixels.

The correlation mapping method is applied to different PIV image pairs, obtained either experimentally or synthetically, and the results are compared with sub-pixel curve fitting methods using both parabolic and Gaussian fits. In all cases CMM greatly reduces the peak-locking bias, and also reduces the random error. Application of CMM-PID on experimental turbulence images gives more balanced sub-pixel displacement histograms. The chequered pattern in vorticity distribution caused by peak-locking bias is also significantly reduced. CMM also performs better in noisy images.

Before concluding, one should be reminded that the ± 0.01 pixels uncertainty and bias-free results are obtained using 2D synthetic images. Out-of-plane motion, non-uniform particle distributions within an interrogation window and noise will degrade the measurement accuracy in experimental data.

Appendix A. Evaluation of interpolation schemes

As addressed in many studies, a good sub-pixel interpolation scheme should avoid the loss, addition and biasing of image information (e.g. Scarano 2002). For the specific application in PIV, the centre location of the interpolated particle must be accurately reproduced without bias. In order to select an optimal interpolation method, we apply them on synthetic images, which simulate sub-pixel translation of an individual particle. We use a particle with a Gaussian greyscale intensity distribution (Raffel *et al* 1998):

$$g(x, y) = I_0 \exp\left(-\frac{(x - x_0)^2 + (y - y_0)^2}{1/8 d_p^2}\right) \quad \text{(A.1)}$$

where (x_0, y_0) is the particle centre, d_p is the particle diameter and I_0 is the peak density. Our reference consists of two synthetic images displaced by some sub-pixel distance
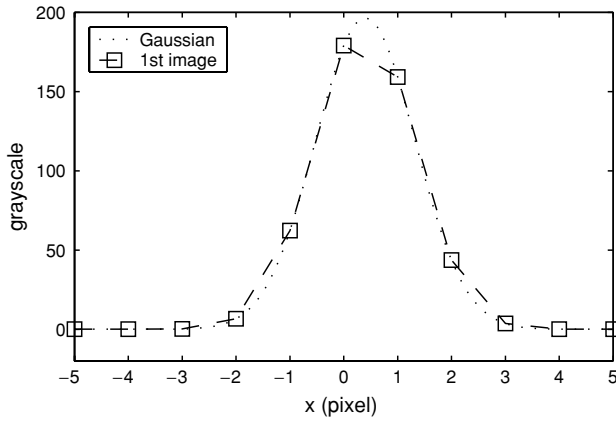
Figure 16. Greyscale distribution across the centre of a Gaussian particle, $d_p = 3.5$ pixels, $I_0 = 240$, located at (0.40, 0.40).

(u, v) using equation (A.1). We also use the bi-linear, bi-parabolic and bi-cubic interpolation methods, to displace the first image by (u, v). The expressions of bi-linear and bi-parabolic interpolation are well documented, e.g. Pozrikidis (1998) and Bracewell (1995), while bi-cubic interpolation is described in equation (6) and appendix B. The intensity distributions obtained using the three interpolation methods are then compared with the exact Gaussian shifted intensity distribution.

Figure 16 shows a 1D cross-section of the first exposure. Figure 17 shows the interpolation errors, i.e. the difference between the interpolated and the exact greyscales, of the particle images displaced by 0.25, 0.50 and 0.75 pixels. The bi-linear interpolation results at the discrete points closest to the peaks ($x = 1$ pixel) are lower than those of the bi-parabolic and bi-cubic greyscales. The errors of the bi-parabolic result in the left and right neighbours of the peak have different signs. For example, in figure 17(a), the greyscale at $x = 0$ is overestimated, while the one at $x = 2$ is underestimated. In figure 17(c), the value at $x = 0$ is underestimated while the value at $x = 2$ is overestimated. The unevenly distributed error creates a bias in the location of the particle centre that depends on the sub-pixel displacement. The bias error associated with bi-parabolic interpolation is even worse than the bi-linear results. To explain the cause for this larger error, note that when the sub-pixel location of the particle centre crosses 0.5, four of the nine pixels used for calculating the bi-parabolic interpolated value change. Thus, bi-parabolic interpolation inherently utilizes pixels that are biased to one of the sides of the particle centre.

Of the three interpolation methods discussed here, the bi-cubic interpolation has the least error, and very little bias with respect to the peak. Since the Gaussian distribution drops drastically beyond twice the particle diameter, this simplified analysis is relevant for typical PIV images containing multiple particles.

Appendix B. Coefficients in bi-cubic interpolation schemes

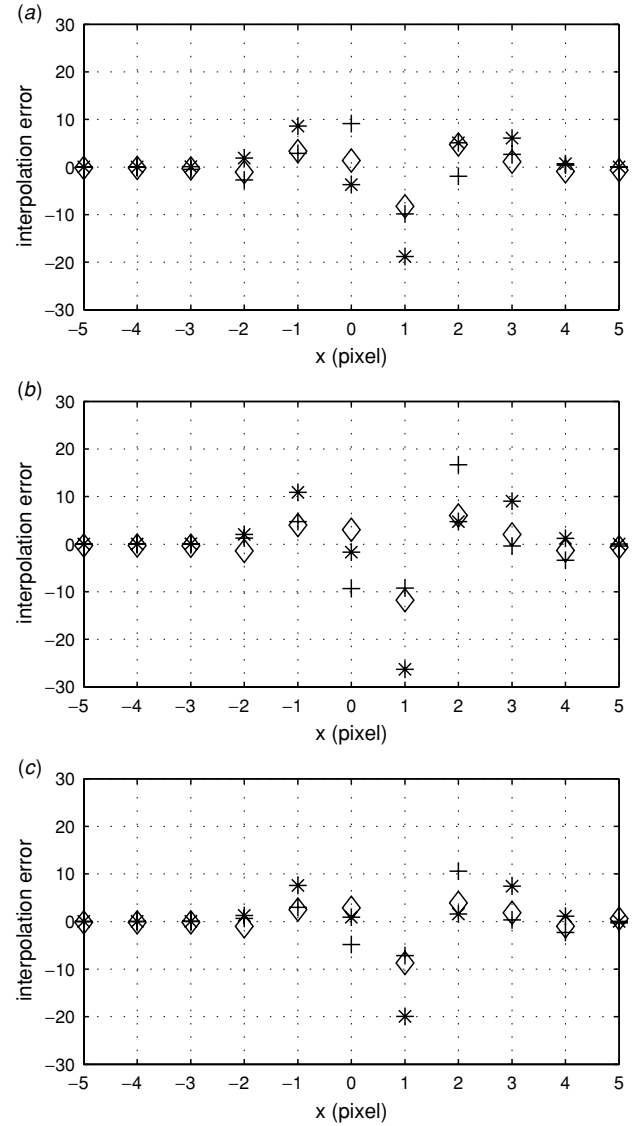The 16 coefficients of the bi-cubic interpolation scheme, equation (6), are:

Figure 17. The interpolation error, i.e. the greyscale difference between the interpolated and exact values, where the particle in figure 16 is displaced horizontally by (a) 0.25 pixels, (b) 0.50 pixels, and (c) 0.75 pixels. Asterisks: bi-linear interpolation, crosses: bi-parabolic interpolation, diamonds: bi-cubic interpolation.

$$
\begin{aligned}
C_1^{(p,q)} ={}& \tfrac{1}{36}g(p-1, q-1) - \tfrac{1}{12}g(p-1, q) \\
&+ \tfrac{1}{12}g(p-1, q+1) - \tfrac{1}{36}g(p-1, q+2) - \tfrac{1}{12}g(p, q-1) \\
&+ \tfrac{1}{4}g(p, q) - \tfrac{1}{4}g(p, q+1) + \tfrac{1}{12}g(p, q+2) \\
&+ \tfrac{1}{12}g(p+1, q-1) - \tfrac{1}{4}g(p+1, q) + \tfrac{1}{4}g(p+1, q+1) \\
&- \tfrac{1}{12}g(p+1, q+2) - \tfrac{1}{36}g(p+2, q-1) + \tfrac{1}{12}g(p+2, q) \\
&- \tfrac{1}{12}g(p+2, q+1) + \tfrac{1}{36}g(p+2, q+2) \\
C_2^{(p,q)} ={}& -\tfrac{1}{12}g(p, q-1) + \tfrac{1}{4}g(p, q) - \tfrac{1}{4}g(p, q+1) \\
&+ \tfrac{1}{12}g(p, q+2) + \tfrac{1}{6}g(p+1, q-1) - \tfrac{1}{2}g(p+1, q) \\
&+ \tfrac{1}{2}g(p+1, q+1) - \tfrac{1}{6}g(p+1, q+2) \\
&- \tfrac{1}{12}g(p+2, q-1) + \tfrac{1}{4}g(p+2, q) - \tfrac{1}{4}g(p+2, q+1) \\
&+ \tfrac{1}{12}g(p+2, q+2)
\end{aligned}
$$

$$C_3^{(p,q)} = -\tfrac{1}{12}g(p-1,q) + \tfrac{1}{6}g(p-1,q+1)$$
$$-\tfrac{1}{12}g(p-1,q+2) + \tfrac{1}{4}g(p,q) - \tfrac{1}{2}g(p,q+1)$$
$$+\tfrac{1}{4}g(p,q+2) - \tfrac{1}{4}g(p+1,q) + \tfrac{1}{2}g(p+1,q+1)$$
$$-\tfrac{1}{4}g(p+1,q+2) + \tfrac{1}{12}g(p+2,q) - \tfrac{1}{6}g(p+2,q+1)$$
$$+\tfrac{1}{12}g(p+2,q+2)$$

$$C_4^{(p,q)} = +\tfrac{1}{4}g(p,q) - \tfrac{1}{2}g(p,q+1) + \tfrac{1}{4}g(p,q+2)$$
$$-\tfrac{1}{2}g(p+1,q) + g(p+1,q+1) - \tfrac{1}{2}g(p+1,q+2)$$
$$+\tfrac{1}{4}g(p+2,q) - \tfrac{1}{2}g(p+2,q+1) + \tfrac{1}{4}g(p+2,q+2)$$

$$C_5^{(p,q)} = -\tfrac{1}{36}g(p-1,q-1) + \tfrac{1}{12}g(p-1,q)$$
$$-\tfrac{1}{12}g(p-1,q+1) + \tfrac{1}{36}g(p-1,q+2) + \tfrac{1}{6}g(p,q-1)$$
$$-\tfrac{1}{2}g(p,q) + \tfrac{1}{2}g(p,q+1) - \tfrac{1}{6}g(p,q+2)$$
$$-\tfrac{1}{12}g(p+1,q-1) + \tfrac{1}{4}g(p+1,q) - \tfrac{1}{4}g(p+1,q+1)$$
$$+\tfrac{1}{12}g(p+1,q+2) - \tfrac{1}{18}g(p+2,q-1) + \tfrac{1}{6}g(p+2,q)$$
$$-\tfrac{1}{6}g(p+2,q+1) + \tfrac{1}{18}g(p+2,q+2)$$

$$C_6^{(p,q)} = -\tfrac{1}{36}g(p-1,q-1) + \tfrac{1}{6}g(p-1,q)$$
$$-\tfrac{1}{12}g(p-1,q+1) - \tfrac{1}{18}g(p-1,q+2) + \tfrac{1}{12}g(p,q-1)$$
$$-\tfrac{1}{2}g(p,q) + \tfrac{1}{4}g(p,q+1) + \tfrac{1}{6}g(p,q+2)$$
$$-\tfrac{1}{12}g(p+1,q-1) + \tfrac{1}{2}g(p+1,q) - \tfrac{1}{4}g(p+1,q+1)$$
$$-\tfrac{1}{6}g(p+1,q+2) + \tfrac{1}{36}g(p+2,q-1) - \tfrac{1}{6}g(p+2,q)$$
$$+\tfrac{1}{12}g(p+2,q+1) + \tfrac{1}{18}g(p+2,q+2)$$

$$C_7^{(p,q)} = -\tfrac{1}{6}g(p+1,q-1) + \tfrac{1}{2}g(p+1,q)$$
$$-\tfrac{1}{2}g(p+1,q+1) + \tfrac{1}{6}g(p+1,q+2)$$

$$C_8^{(p,q)} = -\tfrac{1}{6}g(p-1,q+1) + \tfrac{1}{2}g(p,q+1)$$
$$-\tfrac{1}{2}g(p+1,q+1) + \tfrac{1}{6}g(p+2,q+1)$$

$$C_9^{(p,q)} = +\tfrac{1}{12}g(p-1,q) - \tfrac{1}{6}g(p-1,q+1)$$
$$+\tfrac{1}{12}g(p-1,q+2) - \tfrac{1}{2}g(p,q) + g(p,q+1)$$
$$-\tfrac{1}{2}g(p,q+2) + \tfrac{1}{4}g(p+1,q) - \tfrac{1}{2}g(p+1,q+1)$$
$$+\tfrac{1}{4}g(p+1,q+2) + \tfrac{1}{6}g(p+2,q) - \tfrac{1}{3}g(p+2,q+1)$$
$$+\tfrac{1}{6}g(p+2,q+2)$$

$$C_{10}^{(p,q)} = \tfrac{1}{12}g(p,q-1) - \tfrac{1}{2}g(p,q) + \tfrac{1}{4}g(p,q+1)$$
$$+\tfrac{1}{6}g(p,q+2) - \tfrac{1}{6}g(p+1,q-1) + g(p+1,q)$$
$$-\tfrac{1}{2}g(p+1,q+1) - \tfrac{1}{3}g(p+1,q+2)$$
$$+\tfrac{1}{12}g(p+2,q-1) - \tfrac{1}{2}g(p+2,q) + \tfrac{1}{4}g(p+2,q+1)$$
$$+\tfrac{1}{6}g(p+2,q+2)$$

$$C_{11}^{(p,q)} = \tfrac{1}{2}g(p+1,q) - g(p+1,q+1) + \tfrac{1}{2}g(p+1,q+2)$$

$$C_{12}^{(p,q)} = \tfrac{1}{2}g(p,q+1) - g(p+1,q+1) + \tfrac{1}{2}g(p+2,q+1)$$

$$C_{13}^{(p,q)} = +\tfrac{1}{36}g(p-1,q-1) - \tfrac{1}{6}g(p-1,q)$$
$$+\tfrac{1}{12}g(p-1,q+1) + \tfrac{1}{18}g(p-1,q+2) - \tfrac{1}{6}g(p,q-1)$$
$$+ g(p,q) - \tfrac{1}{2}g(p,q+1) - \tfrac{1}{3}g(p,q+2)$$
$$+\tfrac{1}{12}g(p+1,q-1) - \tfrac{1}{2}g(p+1,q) + \tfrac{1}{4}g(p+1,q+1)$$
$$+\tfrac{1}{6}g(p+1,q+2) + \tfrac{1}{18}g(p+2,q-1) - \tfrac{1}{3}g(p+2,q)$$
$$+\tfrac{1}{6}g(p+2,q+1) + \tfrac{1}{9}g(p+2,q+2)$$

$$C_{14}^{(p,q)} = \tfrac{1}{6}g(p+1,q-1) - g(p+1,q) + \tfrac{1}{2}g(p+1,q+1)$$
$$+\tfrac{1}{3}g(p+1,q+2)$$

$$C_{15}^{(p,q)} = \tfrac{1}{6}g(p-1,q+1) - g(p,q+1) + \tfrac{1}{2}g(p+1,q+1)$$
$$+\tfrac{1}{3}g(p+2,q+1)$$

$$C_{16}^{(p,q)} = g(p+1,q+1)$$

References

Adrian R 1991 Particle-imaging techniques for experimental fluids mechanics *Ann. Rev. Fluid Mech.* **23** 261–304

Bracewell R 1995 *Two-Dimensional Imaging* (Englewood Cliffs, NJ: Prentice-Hall)

Chen J, Meneveau C and Katz J 2005 Scale interactions of turbulence subjected to a straining–relaxation–destraining cycle *J. Fluid Mech.* submitted

Christensen K T 2004 The influence of peak-locking errors on turbulence statistics computed from PIV ensembles *Exp. Fluids* **36** 484–97

Fincham A and Delerce G 2000 Advanced optimization of correlation imaging velocimetry algorithms *Exp. Fluids* **29** (Suppl.) S13–22

Fincham A and Spedding G 1997 Low cost, high resolution DPIV for measurement of turbulent fluid flow *Exp. Fluids* **23** 449–62

Florio D, Felice F and Romano G 2002 Windowing, re-shaping and re-orientation interrogation windows in particle image velocimetry for the investigation of shear flows *Meas. Sci. Technol.* **13** 953–62

Foucaut J and Stanislas M 2002 Some considerations on the accuracy and frequency response of some derivative filters applied to particle image velocimetry vector fields *Meas. Sci. Technol.* **13** 1058–71

Gui L and Seiner J M 2004 An improvement in the nine-point central difference image correction method for digital particle image velocimetry recording evaluation *Meas. Sci. Technol.* **15** 1958–64

Gui L and Wereley S 2002 A correlation-based continuous window-shift technique to reduce the peak-locking effect in digital PIV image evaluation *Exp. Fluids* **32** 506–17

Hart D P 2000 PIV error correction *Exp. Fluids* **29** 13–22

Huang H, Diabiri D and Gharib M 1997 On the error of digital particle image velocimetry *Meas. Sci. Technol.* **8** 1427–40

Huang H, Fiedler H and Wang J 1993 Limitation and improvement of PIV: part II. Particle image distortion, a novel technique *Exp. Fluids* **15** 263–73

Keane R and Adrian R 1990 Optimization of particle image velocimeters, part I, double pulsed systems *Meas. Sci. Technol.* **1** 1202–15

Lecordier B *et al* 2001 Estimation of the accuracy of PIV treatments for turbulent flow studied by direct numerical simulation of multi-phase flow *Meas. Sci. Technol.* **12** 1382–91

Lecordier B, Lecordier J and Trinite M 1999 Iterative sub-pixel algorithm for the cross-correlation PIV measurements *Proc. 3rd Int. Workshop on PIV (Santa Barbara)*

Lin H J and Perlin M 1998 Improved methods for thin, surface boundary layer investigations *Exp. Fluids* **25** 431–44

Nogueira J, Lecuona A and Rodriguez P A 2001 Local field correction PIV, implemented by means of simple algorithms, and multigrid versions *Meas. Sci. Technol.* **12** 1911–21

Pozrikidis C 1998 *Numerical Computation in Science and Engineering* (Oxford: Oxford University Press)

Raffel M, Willert C and Kompenhans J 1998 *Particle Image Velocimetry—A Practical Guide* (Berlin: Springer)

Roesgen T 2003 Optimal subpixel interpolation in particle image velocimetry *Exp. Fluids* **35** 252–6

Roth G and Katz J 2001 Five techniques for increasing the speed and accuracy of PIV interrogation *Meas. Sci. Technol.* **12** 238–45

Roth G, Mascenik D and Katz J 1999 Measurements of the flow structure and turbulence within a ship bow wave *Phys. Fluids* **11** 3512–23

Scarano F 2002 Iterative image deformation methods in PIV *Meas. Sci. Technol.* **13** R1–19

Scarano F and Riethmuller M L 2000 Advances in iterative multigrid PIV image processing *Exp. Fluids* **29** (Suppl.) S51–60

Stanislas M, Okamoto K and Kahler C 2003 Main results of the first international PIV challenge *Meas. Sci. Technol.* **14** R63–89

Teuber J 1993 *Digital Image Processing* (Harlow, UK: Prentice-Hall International)

Wereley S T and Gui L 2003 A correlation-based central difference image correction (CDIC) method and application in a four-roll mill flow PIV measurement *Exp. Fluids* **34** 42–51

Wereley S T and Meinhart C C 2001 Second-order accurate particle image velocimetry *Exp. Fluids* **31** 258–68

Westerweel J 1997 Fundamentals of digital particle image velocimetry *Meas. Sci. Technol.* **8** 1379–92

Willert C and Gharib M 1991 Digital particle image velocimetry *Exp. Fluids* **10** 181–93